J. Fluid Mech. (2004), *vol.* 510, *pp.* 243–265.
DOI: 10.1017/S002211200400953X Printed in the United Kingdom

Instability of convection of an ethanol–water solution in a vertical tank

By CHO LIK CHAN, YOUMIN YU AND C. F. CHEN

Department of Aerospace and Mechanical Engineering, University of Arizona, Tucson, AZ, 85721, USA

(Received 25 June 2003 and in revised form 25 February 2004)

An experimental and numerical investigation has been carried out into the instability characteristics of natural convection of an ethanol–water solution in a vertical tank with aspect ratio (height/width) of 15. The solution contains 39 wt% ethanol with Prandtl number $Pr = 26$. The density anomaly due to the Soret effect may be safely ignored in the present test configuration. Onset of instability, in the form of multicellular convection located in the mid-height of the tank, occurs at Grashof number $Gr \cong 13\,500$. These convection cells are unsteady even at low supercritical states, similar to earlier observations for higher Pr fluids. The cause of such unsteadiness of the flow has been determined by studying the streak images constructed by superposing individual frames of a digital movie sequence. New cells are generated in the upper and lower portions of the tank and then migrate toward the centre, causing the convection cells in the mid-section to merge. At higher Gr, even the tertiary cells, which rotate in the opposite direction of the secondary cells, participate in the merging process. Numerical simulations of the two-dimensional natural convection of a Boussinesq fluid with constant thermophysical properties, carried out at low supercritical Gr equivalent to the experimental value, show the same process of cell generation and merging as that observed in the experiments. By analysing the substantial time rate of change of the kinetic energy of the fluid using the mechanical energy equation, it is determined that the energy needed for the cell generation process is supplied by the work of the dynamic pressure. The subsequent migration of the cells toward the middle is caused by the pressure gradient in the tank. The total kinetic energy of the fluid attains a relative maximum right after a merging process due to the reduction of dissipation associated with the region of strong shear between the cells.

1. Introduction

According to linear stability analysis of natural convection in an infinite vertical slot, the mode of instability onset depends on the Prandtl number of the fluid. For fluids with $Pr < 12.5$, the instability onset is in the steady convection mode and the critical Grashof number is independent of Pr. The analyses of Vest & Aparci (1969) and Gill & Kirkham (1970) yield a critical value of $Gr \cong 7900$, which is correct to within a few percent for all Prandtl numbers. For fluids with $Pr > 12.5$, however, the onset is in the oscillatory or travelling mode and the critical Grashof number decreases with increasing Pr. Gill & Kirkham (1970) gave the result $Gr \cong 9400 Pr^{-1/2}$. It is noted here that the value of 12.5 is based on the more recent and more accurate stability analysis of Chen & Pearlstein (1989). A number of experiments with air,

water and fluids with $Pr > 12.5$ have been carried out by a number of investigators, with varying degrees of disagreement with the predictions above.

For air, Vest & Arpaci (1969) found the onset of instability is in the multicellullar mode at the critical value $Gr \cong 8700$ in a tank with aspect ratio (height to width) $A = 33.3$. Hollands & Konicek (1973) found a higher critical value of $Gr \cong 11\,000$ with $A = 44$. These results are 10–40% higher than the predicted value. For water, however, with $Pr = 6.7$, Hart (1971) found that onset is in the form of transverse travelling waves at $Gr \cong 14\,900$ with $A = 37$. At $A = 25$, Gr increases to $\sim 19\,400$. These values are higher than the predicted value, however, they are in fair agreement with the results of linear stability theory in which the vertical temperature gradient in the tank is taken into account (Hart 1971). Bergholz (1978) analysed the instability problem with temperature stratification as a parameter and presented results for fluids with $Pr = 0.73$ to 1000. The results show that, for low to moderate values of Pr, the onset of instability will change from the stationary mode to the travelling-wave mode if the stratification is large enough. For high Pr fluids, however, the transition is from the travelling-wave mode to the stationary mode with increasing stratification. Most of Bergholz's linear stability results are confirmed by the recent nonlinear analysis of Christov & Homsy (2001).

There have been a number of experiments carried out using fluids with $Pr \geqslant 50$, especially for fluids with very high Prandtl numbers in tall narrow tanks with aspect ratios $A \geqslant 15$. The first onset of instability reported by the various investigators is always in the stationary multicellular convection mode. Presumably, the stratification parameters in each of the experiments were high enough that the travelling mode was suppressed. The high stratification parameters may have resulted from the limited aspect ratios of the experimental tanks, as predicted by Daniels (1987) for large Pr fluids. Elder (1965*a*, *b*) reported interesting transition states as Gr is increased. First, the appearance of multiple secondary cells after the critical state is reached, then the onset of tertiary cells in between the secondary cells rotating in the opposite direction, then travelling waves along both walls, and, finally, turbulence. His experiments were carried out for a $Pr \cong 1000$ fluid in a tank with $A = 19$. Other results were reported for fluids of different Pr, all $\geqslant 50$ (Vest & Arpaci 1969; Seki, Fukusako & Inaba 1978; Chen & Thangam 1985; Wakitani 1994).

Wakitani (1996) studied fluids with $Pr = 125$ and 900 in a tank of $A = 15$. It was found that, contrary to what had been reported before, the secondary flow of multiple convections cells is unsteady, even at low supercritical states. The convection cells are constantly moving and merging. Previous investigators, including ourselves, missed this phenomenon, probably because of the flow visualization technique used. He also carried out numerical simulations of the same cases, showing the same unsteady processes as observed in the experiments. We have recently concluded an experimental and numerical study of the stability of convection of an ethanol–water solution with $Pr = 26$ in a tank of $A = 15$ for the purpose of establishing a database of such a system under steady gravity for comparison with planned experiments of the same system under gravity modulation. We also found cell merging processes in low supercritical states. Convection cells are generated in the upper and lower portions of the tank, and they grow as they migrate toward the centre and cause the merging of cells in the middle of the tank. These processes occur periodically, resulting in a continuing unsteady state of motion in the tank. The frequency of the merging processes is approximately 20 times smaller than that predicted for the travelling wave instability. These are two distinct modes of instability, even though both are time-varying. By analysing the time rate of change of the kinetic energy of

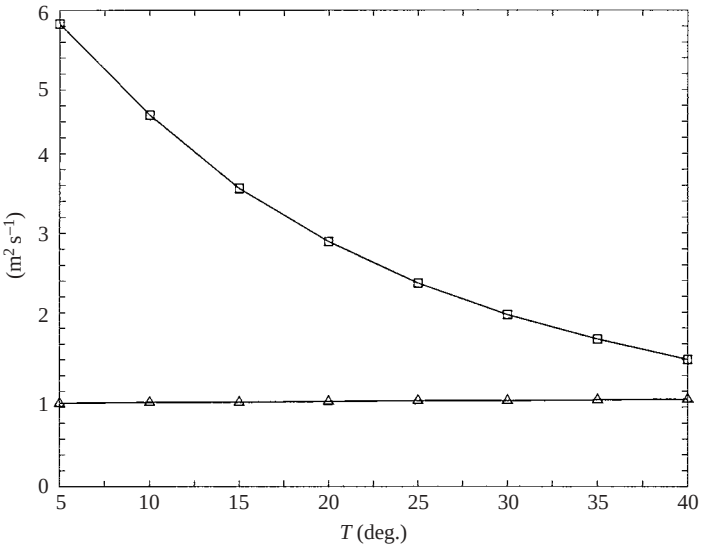

FIGURE 1. Variations of ν and κ with temperature for a 39% ethanol–water solution. □, $\nu \times 10^6$; △, $\kappa \times 10^7$.

the fluid, the energy source responsible for such cell genesis processes was identified. In the following, the experimental apparatus and procedure are presented in § 2, the methods of numerical simulations in § 3, experimental and simulation results §§ 4 and 5, kinetic energy considerations in § 6, and the results are summarized in § 7.

2. Experimental apparatus and procedure

The experiments were conducted in a tall tank with interior dimensions of 225 mm high × 15 mm wide × 75 mm deep. The two tall sidewalls are made of aluminium of thickness 12.5 mm in which passages are provided for the circulation of constant-temperature fluids supplied by two constant-temperature baths. Both are sealed by Plexiglas backing. All other walls are 12.5 mm thick Plexiglas for flow-visualization purposes. Five thermocouples are embedded 45 mm apart along the vertical centreline of each of the heat transfer walls, starting 25 mm from the top. These thermocouples are installed approximately 1.6 mm from the interior surface. It is estimated by a heat transfer analysis that the difference between the measured temperature and that of the inner surface is $0.002\Delta T$ across the tank owing to the large heat conductivity of aluminium. The temperature signals are processed and analysed by using the software package LabVIEW (Version 6i).

The working fluid is a 39% by weight ethanol–water solution. Its thermophysical properties can be found in Landolt & Bornstein (1989). At 22 °C, the kinematic viscosity $\nu = 2.846 \times 10^{-6}\,\mathrm{m^2\,s^{-1}}$, thermal diffusivity $\kappa = 0.107 \times 10^{-6}\,\mathrm{m^2\,s^{-1}}$, and thermal expansion coefficient $\beta = 0.785 \times 10^{-3}\,\mathrm{K^{-1}}$. The viscosity and thermal expansion coefficient are approximately three times those of water. The variations of these properties with temperature in the range of 5 °C–40 °C are shown in figure 1. The Soret effect in the ethanol–water solution may be safely ignored since its effect on the density change is very small (approximately 10^{-3}) compared to the direct effect of temperature. For flow-visualization and PIV purposes, the fluid is seeded with 10 μm polycrystalline particles. A Coherent 4 W laser provides the light source, which is rendered into a light sheet approximately 1 mm thick by a cylindrical lens.

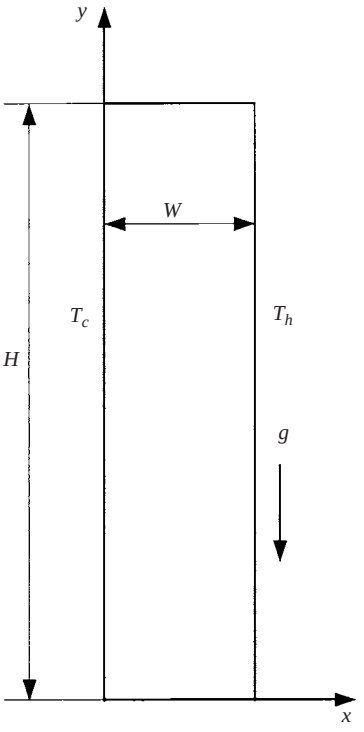

FIGURE 2. Coordinate system.

Through a deflecting mirror, the light sheet is made to shine vertically downward in order to illuminate the midplane of the convection tank. The motion of the particles is captured by a Pixelink digital movie camera with a frame rate of 9 f.p.s. The digital data are streamed into a Power Macintosh computer for flow analysis and visualization purposes.

To start the experiment, the test tank is filled with an ethanol–water solution seeded with particles. After the initial motion has subsided, circulation of the fluids from the two constant-temperature baths, set at predetermined T_h and T_c, is started through the two heat transfer walls, thus beginning the experiment. In all cases, $T_{h,c} = T_r \pm \Delta T/2$, where T_r is the reference temperature, usually set at 22 °C. All thermophysical properties are evaluated at T_r. Data are taken at 20 min after the start of the experiment, or after a new setting of ΔT. This is about twice the thermal diffusion time for half the tank width, 7.5 mm. Digital movies are recorded for 5–20 min intervals. In order to visualize the convection cells in the tank, streaklines are constructed by superposing consecutive movie frames for a time lapse of 4.5 s unless otherwise noted.

3. Numerical simulations and kinetic energy considerations

Consider two-dimensional natural convection of a Newtonian fluid of constant thermophysical properties in a vertical tank of height H and width W. The left-hand and right-hand sidewalls are held at constant temperatures, T_c and T_h ($> T_c$), while the top and bottom boundaries are adiabatic. Let the x- and y-coordinates be in the horizontal and vertical directions, as shown in figure 2. Using the Boussinesq approximation, the basic equations in non-dimensional form written in terms of the

streamfunction ψ and the vorticity ω are

$$\frac{\partial \omega}{\partial t} = \frac{Gr}{A}\left(\frac{\partial \psi}{\partial x}\frac{\partial \omega}{\partial y} - \frac{\partial \psi}{\partial y}\frac{\partial \omega}{\partial x}\right) + \left(\frac{\partial^2 \omega}{\partial x^2} + \frac{1}{A^2}\frac{\partial^2 \omega}{\partial y^2}\right) + \frac{\partial \theta}{\partial x}, \tag{1}$$

$$\frac{\partial \theta}{\partial t} = \frac{Gr}{A}\left(\frac{\partial \psi}{\partial x}\frac{\partial \theta}{\partial y} - \frac{\partial \psi}{\partial y}\frac{\partial \theta}{\partial x}\right) + \frac{1}{Pr}\left(\frac{\partial^2 \theta}{\partial x^2} + \frac{1}{A^2}\frac{\partial^2 \theta}{\partial y^2}\right), \tag{2}$$

$$\frac{\partial^2 \psi}{\partial x^2} + \frac{1}{A^2}\frac{\partial^2 \psi}{\partial y^2} = -\omega, \tag{3}$$

where

$$u = \frac{1}{A}\frac{\partial \psi}{\partial y}, \quad v = -\frac{\partial \psi}{\partial x}, \quad \omega = \frac{\partial v}{\partial x} - \frac{1}{A}\frac{\partial u}{\partial y}. \tag{4}$$

In these equations, the Grashof number Gr, the Prandtl number Pr, and the aspect ratio A are defined as

$$Gr = \frac{g\beta \Delta T W^3}{\nu^2}, \quad Pr = \frac{\nu}{\kappa}, \quad A = \frac{H}{W}. \tag{5}$$

The scaling quantities to render these equations non-dimensional are W for the horizontal length, AW for the vertical length, W^2/ν for time, and $Gr\nu/W$ for velocity. The non-dimensional temperature θ is defined as $(T - T_r)/\Delta T$. The boundary conditions are

$$\left.\begin{aligned} \psi = \frac{\partial \psi}{\partial x} = 0, \qquad & \theta = -0.5, 0.5 \quad \text{at} \quad x = 0, 1, \\ \psi = \frac{\partial \psi}{\partial y} = \frac{\partial \theta}{\partial y} = 0 \qquad & \text{at} \quad y = 0, 1. \end{aligned}\right\} \tag{6}$$

The initial state is usually quiescent and at the reference temperature.

The numerical solution method is based on the scheme by Lee & Korpela (1983) and used by Jin & Chen (1996). The equations are discretized by the nine-point method of Arakawa (1966) for the nonlinear terms, the DuFort–Frankel method (Dufort & Frankel 1953) for the diffusion terms, and the central-difference method for the time derivatives. The Poisson equation is solved by a fast Fourier solution technique using the fourth-order-accurate nine-point finite-difference scheme of Houstis & Papatheodorou (1979). (The software for this program is available online at http://www.netlib.org; the name of the source code is 'toms/543.') The boundary vorticity is determined by Thom's rule (Roache 1982). The overall scheme is second-order accurate in both time and space. The program is usually run with 65 $(x) \times 1025\,(y)$ grid points, at $\Delta t = 0.0001$ on a PC. It takes approximately 17 h of real-time to reach steady state at a non-dimensional time of 20 ($\sim$ 26 min real-time).

The final code is validated by comparing with the earlier results of Ghia, Ghia & Shin (1982) for a driven cavity and of Le Quéré (1990) for natural convection of air in a tank of aspect ratio 16. For the driven cavity problem, Ghia *et al.* used a coupled strongly implicit multi-grid method for the solution of the problem. The vorticity along the top boundary moving with a Reynolds number of 1000 in a square cavity calculated by the present method is compared with those of Ghia *et al.* in table 1. A grid size of 129×129 is used in both methods. The average difference is 1.4%. For the natural convection of air at $Gr = 33\,800$, Le Quéré used the Tau–Chebyshev algorithm. His results of the streamfunction at the centre of the cavity and the vorticity at the mid-height of the sidewall are compared with the results of

	x						
	0.125	0.250	0.375	0.500	0.625	0.750	0.875
Ghia *et al.* (1982)	51.056	32.295	20.267	14.890	14.137	16.047	23.871
Present study	51.669	32.788	20.644	15.003	14.053	15.840	23.251
Difference (%)	1.200	1.526	1.863	0.759	0.597	1.290	2.596

TABLE 1. Vorticity ω along the moving boundary of the driven flow in a square cavity at $Re = 1000$. Difference $= |\omega_1 - \omega_2|/\omega_1$.

	$\lvert\psi\rvert \times 10^3$	$\omega \times 10^2$	Grids
Le Quéré (1990)	1.316	5.080	32×150
Jin & Chen (1996)	1.317	5.159	33×257
Present study	1.330	5.091	33×513

TABLE 2. Streamfunction ψ at the centre of the slot and vorticity ω at the mid-height of the sidewall for $Ra = 24\,000$, $Pr = 0.71$ and $A = 16$.

the current study, as well as with those of Jin & Chen (1996), in table 2. Again, the differences are approximately 1%. It is noted that the current method differs from that of Jin & Chen only in one respect, the solution scheme of the Poisson equation.

Once the solution is obtained, we consider the rate of change of the kinetic energy of the fluid. By forming the dot product of the velocity vector $\boldsymbol{q}$ with the momentum equation, we obtain the substantial derivative of kinetic energy in non-dimensional form:

$$\frac{\mathrm{D}(KE)}{\mathrm{D}t} = \boldsymbol{q}\cdot\boldsymbol{j}\theta - Gr\,\boldsymbol{q}\cdot\nabla p + \boldsymbol{q}\cdot\nabla^2\boldsymbol{q} = v\theta - Gr\left\{u\frac{\partial p}{\partial x} + v\frac{\partial p}{A\partial y}\right\} + \{u\nabla^2 u + v\nabla^2 v\}, \tag{7}$$

in which p is the dynamic pressure and $\nabla^2 = \partial^2/\partial x^2 + A^{-2}(\partial^2/\partial y^2)$. The three terms on the right-hand side of the equation are the buoyancy work, the pressure work and the shear work, respectively. The last work term can be decomposed into a dissipation term and a diffusion of kinetic energy term. To obtain the time rate of change of the fluid kinetic energy at a given point, the three work terms are computed numerically from the solutions of u, v, θ and ∇p. All numerical schemes used are second-order accurate. All our numerical investigations are limited to moderate Grashof numbers for which the relative viscosity variations in the tank are within ~25%.

4. Experimental results

Experiments were conducted for a range of Gr from ~1600 to ~100 000. It was found that the onset of instability is in the form of multiple secondary convection cells in the tank. The cells, once formed, are constantly merging, as noted by Wakitani (1996) in his experiments with higher Pr fluids. At higher Gr, tertiary cells with circulatory motion opposite to that in the secondary cells started to appear, and they also participated in the merging process. At even higher Gr, secondary cells started to appear in tandem. Upon further increases of Gr, travelling waves appear. Then, the motion in the tank becomes turbulent. These phenomena are each discussed in more detail in the following sections. The test conditions of the experiments selected to be discussed in this section are summarized in table 3. In this table, the temperature stratifications as measured along the hot and cold walls are also included. The

Gr	Pr	ΔT_{cold} (deg)	ΔT_{hot} (deg)	ΔT (deg)
11 700	26.16	0.09	0.48	3.46
13 000	26.09	0.14	0.53	3.61
14 300	26.16	0.14	0.58	4.04
20 200	26.15	0.23	0.74	5.99
53 900	26.23	0.85	1.92	16.08
64 400	26.19	1.07	2.31	19.16
77 400	26.19	1.19	2.87	23.35
99 300	26.00	1.52	3.58	29.02

TABLE 3. Experimental conditions for selected experiments. ΔT_{cold} and ΔT_{hot} are the temperature differences between the top and bottom thermocouples in the cold and hot sidewalls. ΔT is the temperature difference across the sidewalls at the mid-height of the tank.

stratification is larger along the hot wall than along the cold wall. Consequently, ΔT across the tank near the top (bottom) is approximately 3–5% higher (lower) than that at the mid-tank, depending on the values of ΔT.

4.1. *The critical state*

The first set of experiments was conducted to determine the critical conditions for the onset of instabilities. According to linear stability analysis for convection in an infinite slot, the first instability onset is in the oscillatory mode. For a fluid with $Pr = 25$, the critical Grashof number is 1888, with a critical wavenumber of 1.8 oscillating at a critical frequency of 27.2 (Chen & Chen 1999). Bergholz (1978) considered fluids of $Pr = 20$ and 50 and found that, in the former, the travelling mode of instability remained critical, irrespective of the stratification parameter. For the latter case, the stationary mode of instability became the critical mode over a limited range of stratification parameters and the critical Grashof numbers were only slightly lower than those of the travelling mode. It is surmised from these results that stratification will not affect the linear stability predictions for a $Pr = 26$ fluid as used in the experiment.

Experiments were conducted starting with low $Gr = 1600$, with an incremental Gr of $\sim$1000. At low Grashof numbers, the flow in the tank consists of a single convection cell. No oscillatory instability was detected by monitoring either the flow field or by the temperature at a point near the wall in the tank. As ΔT was gradually increased, the flow in the mid-section of the tank took on the nature of a boundary layer. The first instability detected was the development of multicellular convection when the Grashof number reached between 13 000 and 14 000, as shown in figure 3. In this figure, three particle streak images recorded at $Gr = 11\,700$, 13 000 and 14 300 are shown. The field of view is the middle 7.5 cm of the test tank, with heating on the right-hand wall and cooling on the left-hand wall. At the lowest Gr, the flow is in the boundary-layer regime, with fast-moving fluids near the constant-temperature boundaries and nearly stationary region in the middle of the tank. At $Gr = 13\,000$, there is a hint of cellular motion, but by $Gr = 14\,300$, convection cells can be clearly observed. The same transition range was detected in experiments conducted with impulsively imposed ΔT to reach the final Gr. The experimental critical Gr_{CE} is set at $13\,500 \pm 500$. The wavelength of the cells is approximately $1.66W$, resulting in a critical wavenumber k of 3.8. The linear stability analysis of the initial conduction state also predicts an instability branch that onsets into steady multicellular convection with $Gr_c = 7850$ and $k_c = 2.8$ (Chen & Chen 1999).

FIGURE 3. Streak images of flow in the mid-section of the tank. (*a*) $Gr = 11\,700$, boundary layer flow; (*b*) $Gr = 13\,000$, transitional flow; (*c*) $Gr = 14\,300$, multicellular flow.

We assembled 15 sets of experimental data from a number of studies with fluids of Prandtl numbers varying from 0.71 (air) to 12 500 (glycerine). Of the total, 9 data sets were obtained in test tanks with aspect ratio $A = 15$. The rest were conducted in tanks of higher aspect ratios ranging from 19 to 44. These data, together with our results, are given in table 4 and are shown graphically in terms of the critical Grashof number as a function of the Prandtl number in figure 4. It is seen that for $Pr \geqslant 50$, a power law correlation

$$Gr_c = 2.0 \times 10^6 Pr^{-1.294}, \tag{8}$$

is capable of giving good estimates of all the data points. For fluids with $Pr < 50$, there are only 5 data points at 3 different Prandtl numbers. The critical Grashof numbers vary from 8700 to 19 400, showing no clear trend.

4.2. *Cell generation and merging at* $Gr = 20\,800 \sim 1.54 Gr_{CE}$

Wakitani (1996) noted in his experiments with $Pr = 125$ and 900 fluids that the convection cells, once formed, are constantly merging. For $Pr = 125$, flow-visualization results obtained at 1.7 times the critical Rayleigh number show such merging in progress. We have observed such cell-merging processes at a very low supercritical $Gr = 15\,800 \sim 1.17 Gr_{CE}$. Also, the merging process persists throughout the Grashof number range we tested until the flow becomes turbulent. A detailed study was carried out at $Gr = 20\,800 \sim 1.54 Gr_{CE}$. A 20 min digital movie focusing on the middle third

	Pr	Gr_C	A
Present study	26	13 500	15
Wakitani (1994)	50	12 000	15
	125	4400	15
	900	320	15
Chen & Thangam (1985)	158	2460	15
	163	2520	15
	405	840	15
	720	460	15
Seki *et al.* (1978)	480	370	15
	12 500	8	15
Elder (1965*a*)	1000	300	19
Hart (1971)	6.7	19 400	25
	6.7	14 930	37
Vest & Arpaci (1969)	0.71	8700	33
	900	410	20
Hollands & Konicek (1973)	0.71	11 000	44

TABLE 4. Summary of experimental critical Grashof numbers and the corresponding Prandtl numbers.

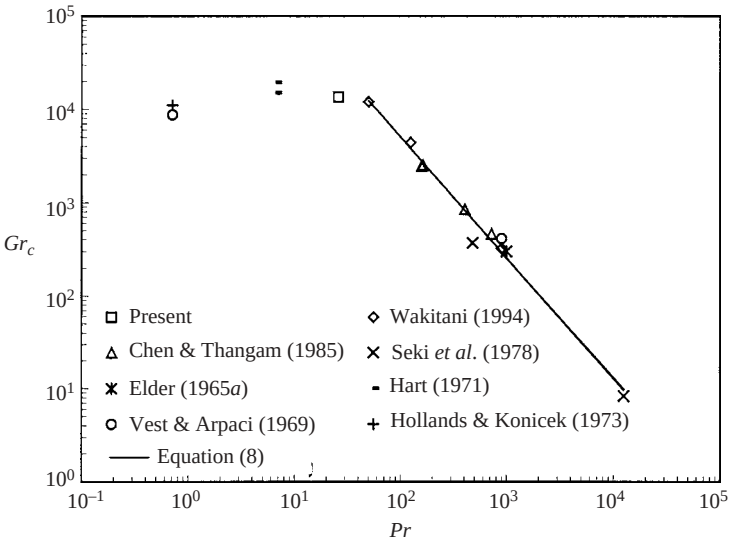

FIGURE 4. Variations of experimental critical Grashof number with Prandtl number. All experiments are performed in tanks with aspect ratio $\geqslant 15$.

of the tank was recorded after the flow had been established at the desired Grashof number for 20 min. A series of 20 streak images constructed at 1 min intervals from the individual frames of the movie is shown in figure 5. The images show that generally there are three convection cells in the field of view, and the flow within each cell is counterclockwise. It can be seen that three separate merging processes occurred within the 20 min period, one each between images 2 and 3, images 9 and 10 and images 17 and 18. Two complete merging cycles occurred between images 3 and 18, with periods of 7 min for the first cycle and 8 min for the second cycle. The actual merging process itself, however, is rapid, generally taking place in 1 min. Because of

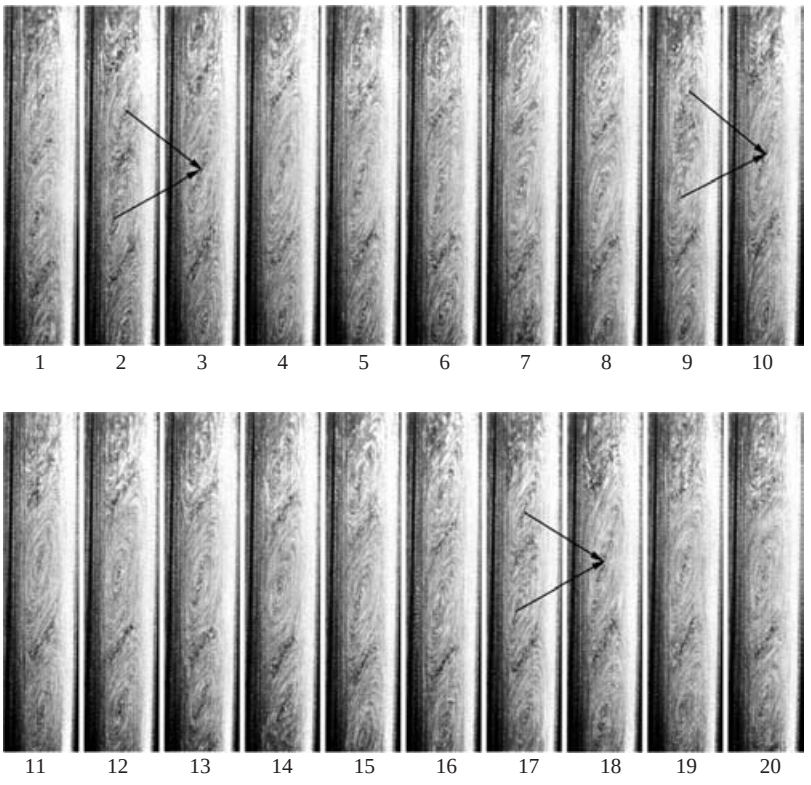

FIGURE 5. Streak images of the flow in the mid-section of the tank at 1 min intervals for $Gr = 20\,800 \sim 1.54Gr_{CE}$ showing three merging processes indicated by arrows.

the unsteady nature of the cell structure, it is difficult to determine the wavenumber of the cells. The centre-to-centre distances between the cells vary between $1.27W$ and $2.13W$, with corresponding wavenumbers 4.95 and 2.95.

Convection cells formed periodically in the upper and lower parts of the tank intrude into the region shown in the figure and squeeze the cells in the middle of the tank, causing them to merge. This can be seen in a sequence of 10 streak images obtained with the camera mounted to view the top third of the tank in a different experiment with $Gr = 20\,200$ shown in figure 6. It should be noted that for this set of experiments, the tank was not well cleaned, leaving a smudge mark approximately 3 mm along the top. It can be seen that the upward flow along the hot wall is turned downward near the top boundary to flow along the cold wall with a characteristic dip. This dip is a prominent feature in the streamline pattern generated from the results of a simulation carried out at a comparable Grashof number, as discussed in § 5. A convection cell can be clearly seen in image 4 near the lower boundary, and it descends out of the field of view by image 8. In image 6, just above the cell under discussion, another cell is forming, and the new cell descends slowly. By image 10, only the upper half remains in view.

4.3. *Tertiary cells at* $Gr = 54\,100 \sim 4Gr_{CE}$

Tertiary cells were first detected at $Gr = 36\,000 Gr \sim 2.67Gr_{CE}$. They were typically elongated convection cells with clockwise rotation situated between the regularly spaced secondary cells with counterclockwise rotation. As Gr is increased, the tertiary

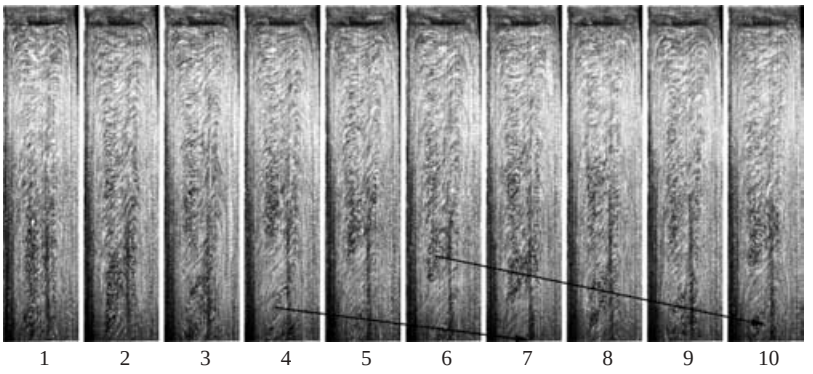

FIGURE 6. Streak images of the flow in the top-section of the tank at 1 min intervals for $Gr = 20\,200$. Note the descent of convection cells into the mid-section below.

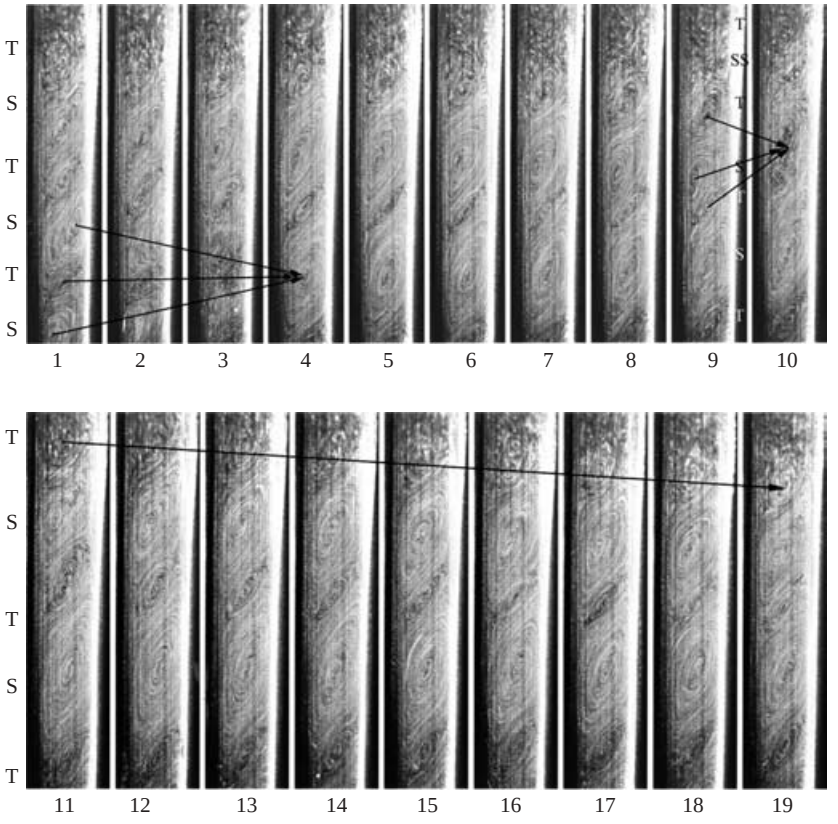

FIGURE 7. Streak images of the flow in the mid-section of the tank at 1 min intervals for $Gr = 54\,100 \sim 4Gr_{CE}$. The six cells shown in the first image are alternately tertiary (T) and secondary (S) from the top. Note the participation of the tertiary cells in the merging process.

cells become larger and eventually participate in the merging process. A series of 19 streak images constructed at 1 min intervals at $Gr = 54\,100 Gr \sim 4Gr_{CE}$ is shown in figure 7 to illustrate the merging phenomenon. In image 1, there are six cells; starting from the top, the cells are alternately tertiary and secondary, with a total of three

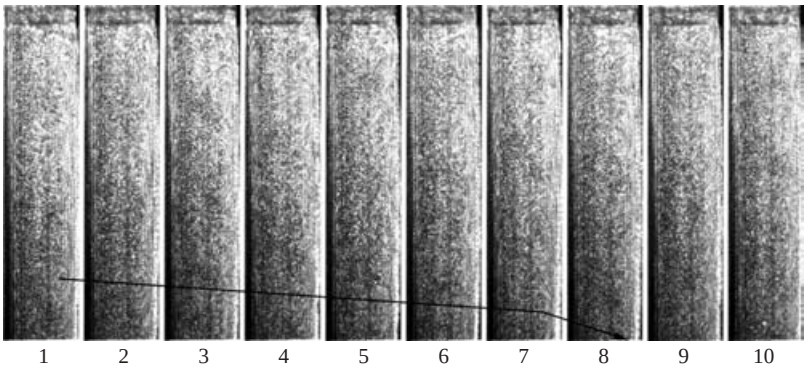

FIGURE 8. Streak images of the flow in the top section of the tank at 1 min intervals for $Gr = 53\,900$. The images are constructed with a 0.6 s exposure. The cells are small and are along the hot wall. The lowest one is seen travelling downward into the mid-section of the tank.

such pairs within the visible region. The sense of rotation of each cell is determined by advancing the movie frames slowly. The bottom three cells merged into one large secondary cell by image 4. The top tertiary cell moved downward towards the middle of the tank owing to the intrusion of cells from the top portion of the tank, and a tertiary cell intruding from the bottom portion of the tank came into view in image 6. Thereafter, the cells continue to move toward the centre. In image 9, the top intrusion developed into a tertiary cell at the top and a tandem pair of secondary cells just below. In the rest of the visible part of the tank, there are five cells, alternately tertiary and secondary from the top. The squeezing motion eventually caused the merging of the middle three cells into a large tertiary cell in image 10, and the tandem pair developed into the full-size secondary cell shown in image 11.

These five cells remained in view for the next 8 min, with the top cell moving slowly downward until the end of the movie segment. It is probable that the three cells in the middle would have merged in the next minute or two. The complete merging cycle occurred between images 4 and 11, with a period of 7 min, the same as in the previous case. The next cycle would have a larger period. At this higher Grashof number, the merging process always involves three cells. Since the vertical arrangement of the cells is alternately secondary and tertiary, any combination of three cells will involve two with the same direction of circulation. When merging, if the three cells include two secondary (tertiary) cells, the final cell is a secondary (tertiary) cell. Now the merging process is a little slower and takes 2 min to accomplish.

A sequence of 10 streak images of the flow in the top part of the tank generated in a different experiment at $Gr = 53\,900$ is shown in figure 8. These images were obtained with a 0.6 s time lapse, and the time interval between images is 1 min. It is seen that there are a number of small convection cells along the hot wall. Similar to the previous case, a convection cell can be seen to descend near the lower boundary, starting with image 1 and disappearing in image 8.

4.4. *Higher Grashof numbers*

Travelling-wave instabilities were first noticed at $Gr = 64\,400 \sim 4.77 Gr_{CE}$. These appear along the hot wall in the upper portion and along the cold wall in the lower portion of the tank. Particles are entrapped in these waves, and, when illuminated by the laser light sheet, they appear as bright lumps ascending rapidly along the hot wall. In figure 9, we show a sequence of ten images that are from every other frame of a

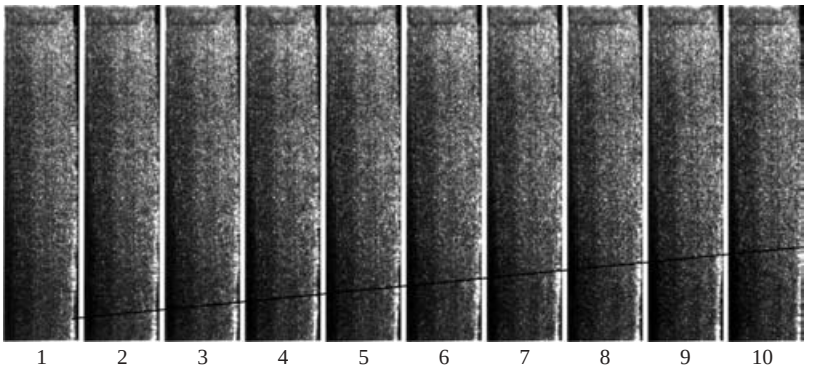

FIGURE 9. Images of the flow in the top-section for $Gr = 64\,400 \sim 4.77Gr_{CE}$ showing an upward-moving travelling wave along the hot wall. The images are obtained by printing every other frame of the digital movie; the time interval between images is $\frac{2}{9}$ s.

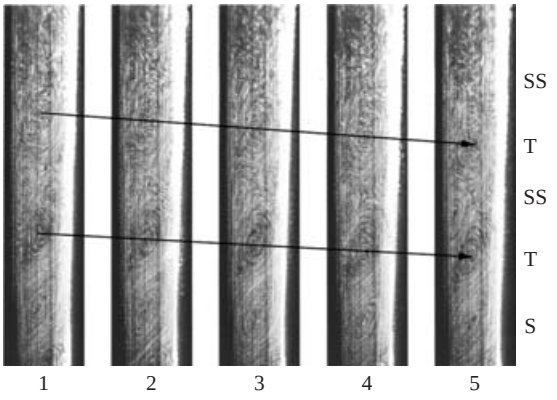

FIGURE 10. Streak images of the flow in the mid-section for $Gr = 77\,400 \sim 5.73Gr_{CE}$ showing the presence of tandem secondary cells indicated by SS.

digital movie segment. The time interval between images is $2/9$ s. In the first image, there are two bright lumps on the lower right-hand side with a third one above, which is ready to break up. We can follow the lowest wave through the ten images as it ascends and obtains a wave speed of approximately $7\,\mathrm{mm\,s^{-1}}$. These waves persist throughout the experiment after the initial transient phase.

As the Grashof number is further increased to $Gr = 77\,400 \sim 5.73Gr_{CE}$, the tandem arrangement of cells first noticed at $Gr = 54\,100$ (figure 7, image 10) becomes more common and prominent in the mid-section of the tank. Five streak images constructed 1 min apart are shown in figure 10. The arrangement of the cells in image 5 from the bottom up is secondary, tertiary, tandem secondary, tertiary and tandem secondary cells. The downward motion of the cells is quite noticeable. At $Gr = 99\,300 \sim 7.36Gr_{CE}$, the flow in the tank becomes turbulent and no coherent streak images are constructed.

5. Simulation results

In this section, we present the simulation results in terms of streamline patterns for cases of moderate Grashof number, comparable to those presented in the experimental

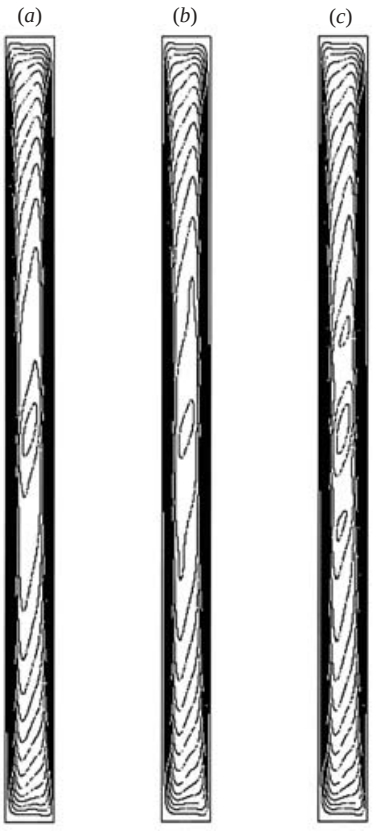

FIGURE 11. Computed streamlines for (*a*) $Gr = 18\,000$, unicellular flow and (*b*), (*c*) $Gr = 19\,000$ at non-dimensional time (*a*) 20, (*b*) 18 and (*c*) 20.25 (~3 min real-time apart) showing the onset of the multicellular flow. Values of the stream function ψ vary from 0 to 2.892×10^{-4} with $\Delta\psi = 1.928 \times 10^{-5}$.

section. All simulations are started from the quiescent state, and the calculations are carried out for 15 non-dimensional time periods (equivalent to 20 min in real-time) before the results are analysed. Many of the salient features observed in the experiments are also obtained in the simulations.

5.1. *The critical state*

Similar to the procedure used in the experiments, calculations were started with a low $Gr = 4000$, then gradually increased to reach the critical state with cellular convection. At low Grashof numbers, the flow in the tank is steady and consists of one single convection cell. The situation remains the same up to $Gr = 18\,000$; a streamline plot for this case is shown in figure 11. In this figure and all the streamline plots to be presented, the hot wall is on the right-hand side. At $Gr = 19\,000$, however, the flow in the tank becomes time-periodic with the convection pattern changing from one to three cells in the tank. Both the one-cell and the three-cell patterns are shown in figure 11. We consider this as the secondary flow regime, and set the critical Grashof number by simulation, $Gr_{CS} = 18\,500$. This value is 37% higher than the experimental value (= 13 500). This discrepancy may occur because the experiments and the simulations are conducted under slightly different conditions. These differences

include (i) temperature gradients along both the heating and cooling walls; (ii) at the critical ΔT, there is a viscosity variation of $\sim 15\%$ from the hot wall to the cold wall; (iii) possible three-dimensional effects in the experiments; and (iv) the background level of disturbances present in the experimental tank is higher than those generated by numerical inaccuracy in the simulations. As for the temperature gradients along the walls, when these conditions were imposed on the simulations, results were not noticeably different from those with constant-temperature boundaries.

We note here that Jin & Chen (1996), by using the same formulation but with a different solver for the Poisson equation and 33×129 grid points, obtained the critical Grashof number ranges of 12 000–13 000 for $Pr = 50$ and 4400–4500 for $Pr = 125$. These agreed well with the experimental results of 12 000 and 4400 obtained by Wakitani (1996). For $Pr = 1000$ fluid, their prediction of the critical Grashof number range of 450–500 is slightly higher than the numerical predictions of Lee & Korpela (1983) of 400. It seems that this simulation method works well for fluids with $Pr \geqslant 50$, but less well for fluids of smaller Pr. Wakitani (1996), using a different numerical scheme but with a non-uniform and non-staggered grid of 31×121, predicted a critical Grashof number of 3056 for $Pr = 125$ that is 31% lower than the experimental value obtain by him two years earlier. Both of these simulations were for constant-property fluids with an aspect ratio of 15 for the tank similar to the present simulation. Our current simulations are carried out with 65×1025 grid points.

In the following, simulations are carried out for $Gr = 30\,000$ to examine the cell merging process. For this case, the simulation Grashof number ratio, $Gr/GR_{CS} = 1.62$, is approximately the same as the experiment carried out at $Gr = 20\,800 = 1.54Gr_{CE}$ for which cell merging was clearly exhibited. At this experimental condition, the corresponding viscosity variation is 21%. Wakitani (1996) performed nonlinear simulations for a supercritical case in which the viscosity variation across the tank is approximately 20%. The simulations were carried out with both constant and variable viscosity assumptions. His results show cell merging in both cases. In particular, he showed that the vertical velocities at the centre of the tank are of the same mean magnitude in both cases. In the variable viscosity case, the time variations of the vertical velocity, which indicate cell merging, show up at earlier times than in the constant viscosity case. Since the purpose of the present simulations is to understand the merging process rather than the exact determination of the merging frequency, we chose to use the constant viscosity assumption in order to reduce the CPU time. Most of the flow characteristics observed in the experiments are reproduced in the simulations.

5.2. *Cell merging at* $Gr = 30\,000 \sim 1.62Gr_{CS}$

Simulations are carried out at $Gr = 30\,000 \sim 1.62Gr_{CS}$ for comparison with the results obtained experimentally at $Gr = 20\,800 \sim 1.54Gr_{CE}$ presented in § 4.2. It is noted that at this experimental Grashof number, the relative viscosity variations in the tank are $\leqslant 25\%$. In figure 12, thirteen streamline patterns at equal time intervals are presented. The first pattern is at non-dimensional time 20.0 (26.3 min), and each subsequent pattern is presented at 0.8 time intervals (1.05 min). For clearer viewing, only the streamline patterns in the top two-thirds of the tank are shown. The streak images presented in figure 5 should be compared with the lower half of the streamline patterns while the images in figure 6 should be compared with those in the top half. First, we note that the general appearance of the convection pattern is similar to that observed in the experiment, as shown in figures 5 and 6. The cell-merging process in the mid-portion of the tank is similar to those shown in figure 5, and

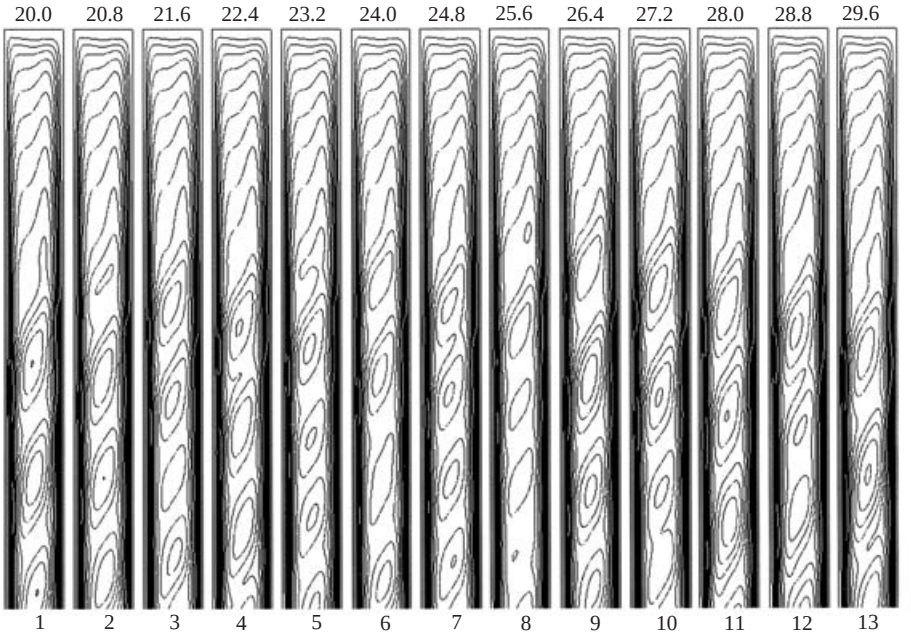

FIGURE 12. Computed streamlines for $Gr = 30\,000 \sim 1.62Gr_{CS}$ at non-dimensional time intervals of 0.8 (~ 1.05 min). For clarity, only the top 2/3 of the tank is shown. Note the migration of cells from both the top and the bottom sections into the mid-section, and the merging of cells in the middle. Values of streamfunction ψ vary from 0 to 2.464×10^{-4} with $\Delta\psi = 1.643 \times 10^{-5}$.

the return flow in the top portion of the tank and the genesis of cells are similar to the images shown in figure 6. Indeed, the centre-to-centre distances between cells range from $1.33W$ to $2.0W$, which compare favourably with the experimental values measure from figure 5 of $1.27W$ to $2.13W$. The migrations of the cells from the top and the bottom parts of the tank toward the centre are clearly exhibited, as is the cell-merging process. However, the merging processes occur more frequently than in the experimental case. Within the 13 patterns presented, there are 5 occurrences of merging, between patterns 3 and 4, 5 and 6, 8 and 9, 10 and 11 and 12 and 13. Similarly, the cell migration process is more rapid in the simulations than in the experiments. The simulation results show similar characteristics to the experiments, but with all the processes happening at a faster pace.

6. Kinetic energy considerations

It is seen that numerical simulations carried out at $Gr = 30\,000 \sim 1.62Gr_{CS}$ yield flow characteristics similar to those observed in the experiment with $Gr = 20\,800 \sim 1.54Gr_{CE}$ but with a different time scale. These include the cell genesis process in the upper and lower sections and the cell merging process in the mid-section. With all the detailed information available from the simulation, we carried out a kinetic energy analysis of the convection system to determine the energy source that causes such processes. From (7), we see that the substantial time rate of change of kinetic energy, $\mathrm{D}(KE)/\mathrm{D}t$, is the sum of the buoyancy work, the pressure work, and the shear work. For the pressure work, the pressure gradient terms are computed by means of the momentum equation. Each of these terms is computed at each node, and the results are then

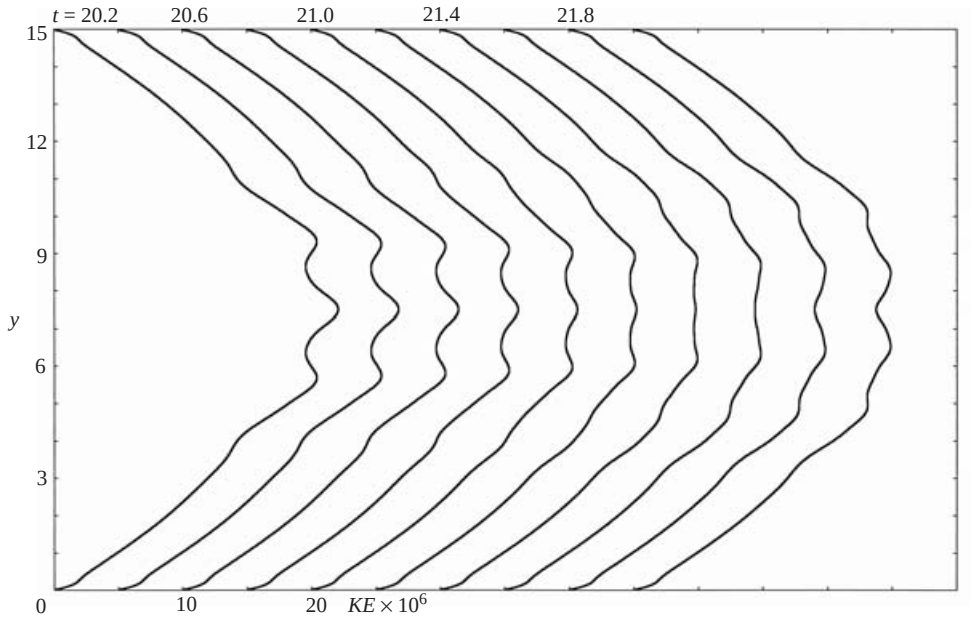

FIGURE 13. Time variations of the computed fluid kinetic energy in the tank for $Gr = 30\,000 \sim 1.62Gr_{CS}$. The non-dimensional time interval between each curve is 0.2 ($\sim$ 16 s). with the origin of each curve offset to the right.

integrated across the tank to obtain the vertical distribution of $\mathrm{D}(KE)/\mathrm{D}t$ in the tank at any time. We focus our attention on the streamline patterns presented in figure 12, particularly the first four panels from $t = 20.0$ to 22.4. Within this short time, cell genesis started at $t = 20$ or earlier, and the completion of cell merging occurred at $t = 22.4$.

6.1. *Cell genesis*

In figure 13, we present the vertical distribution of kinetic energy in the tank at ten time intervals from $t = 20.2$ to 22.0. We note that the small magnitude of the kinetic energy is the result of the velocity scale, which is proportional to the Grashof number. For subcritical convection, the kinetic energy is a symmetric bell-shaped curve with the maximum at the mid-height and $\mathrm{D}(KE)/\mathrm{D}t$ is essentially zero throughout the tank. At supercritical conditions, the circulation in each convection cell will present a local maximum in the KE curve, as is the case in figure 13. At $t = 20.2$, there are three prominent local maxima in the mid-section owing to the three convection cells (see figure 12). Just above and below these cells there are two very small bumps located at $y \cong 3.5$ and 11.5 indicating the onset of convection cells in the upper and the lower potions of the tank; the upper one is visible in the streamline plots shown in figure 12. As time progresses, these two 'young' cells grow larger and migrate toward the centre of the tank.

In order to determine the energy source for this cell genesis process, we examine the vertical distribution of $\mathrm{D}(KE)/\mathrm{D}t$ at time intervals, $t = 18.75$, 19.5 and 20.25 (2 min in real-time), just before the cells become discernible (figure 14). Again, the three centre cells dominate the result, each cell having a large rate of increase for KE. In the top and bottom portions of the tank, the rate of change for KE is nearly zero. We can see, however, the small positive values of $\mathrm{D}(KE)/\mathrm{D}t$ at $y \cong 3.5$ and 11.5 at $t = 18.75$,

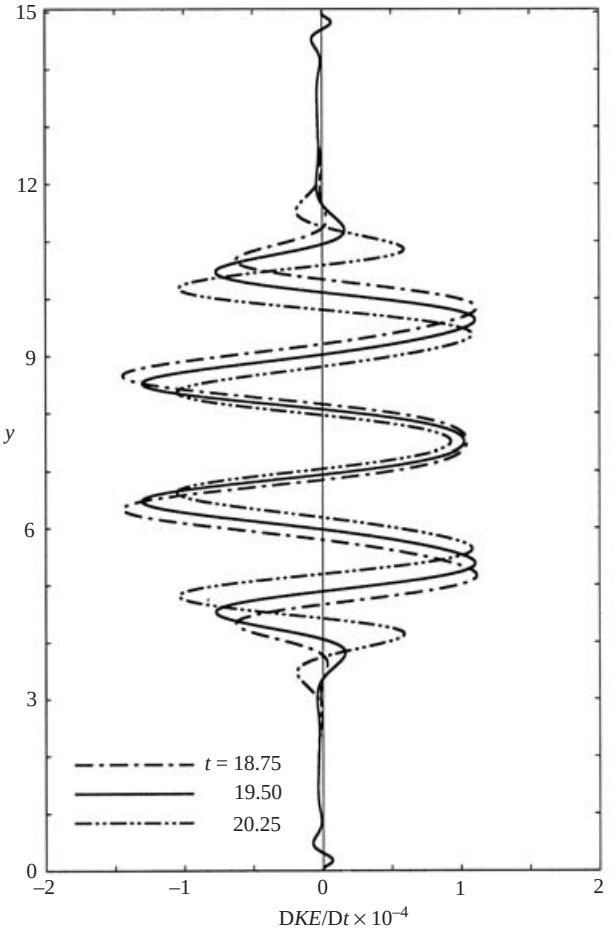

FIGURE 14. Vertical distribution of computed $D(KE)/Dt$ for $Gr = 30\,000$ at $t = 18.75$, 19.5 and 20.25.

signifying the birth of the new cells. In order to examine this in more detail, we show the vertical distributions of the three components that make up $D(KE)/Dt$, the work done by buoyancy, shear and pressure gradient in figure 15. The buoyancy work and the shear work, which are of the same order of magnitude except in sign, are shown in figure 15(*a*), while the pressure work and the sum of the buoyancy and shear work are shown in figure 15(*b*). It is seen that at $y \cong 3.5$ and 11.5 the positive rate of change of kinetic energy is due to the pressure work. This means that small disturbances present in the tank are being amplified by the pressure work to develop into convection cells. Once fully developed, the convection cells are maintained by the buoyancy work since the shear work, being dissipative, is negative.

6.2. *Cell merging*

Within the tank, the pressure is minimum at the centre and maximum at either end. The vertical pressure gradient $\partial p/\partial y$ is shown as a function of y at $t = 21$ just prior to the merging process in figure 16. The general shape of the curve remains the same, with small variations at different times owing to the presence of the convection cells. Cells generated from the two ends migrate down the pressure gradient toward

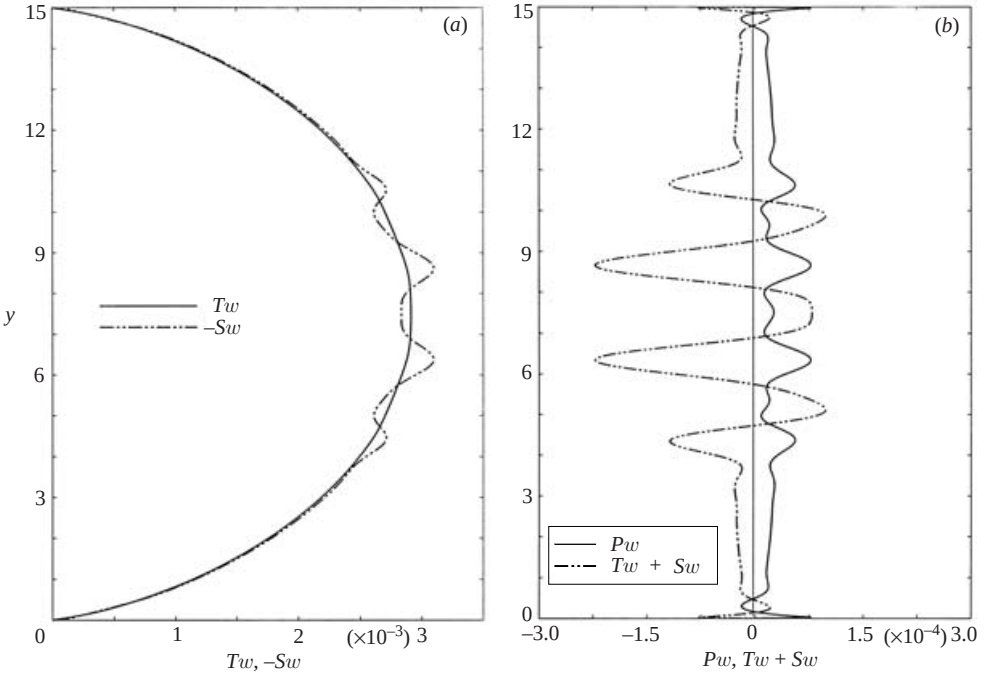

FIGURE 15. Vertical distributions of the work terms at $Gr = 30\,000$ and $t = 18.75$: (*a*) buoyancy work, Tw, and the negative shear work, $-Sw$ and (*b*) pressure work, Pw, and the sum of the buoyancy and shear work ($Tw + Sw$).

the centre, causing the merging of cells in the middle. With each cell-merging, the region of strong shear between the two merging cells vanishes, thereby reducing the dissipation in the tank. As a result, the value of $\mathrm{D}(KE)/\mathrm{D}t$ for the entire tank is increased. For the time period $t = 20$ to 29.6 shown in figure 12, there are five merging processes. When $\mathrm{D}(KE)/\mathrm{D}t$ for the entire tank is shown as a function of time in figure 17, it is seen that the time at each of the five maxima coincides with the time of each merging event.

It can be concluded that the presence of a pressure gradient within the tank is the cause of both cell genesis and the cell-merging process, and the pressure work provided the energy needed for these two processes.

7. Discussions on the absence of travelling-wave instability

Gill (1966) has shown that the boundary layers, which develop along the two vertical walls of the tank, are similar to the buoyancy boundary layers considered by Prandtl (1952) for 'mountain and valley winds'. The linear stability of such buoyancy boundary layers was analysed by Gill & Davey (1969) and extended by Gill & Kirkham (1970) to convection in a vertical tank. Travelling-wave instability was found to be the most critical for fluids of large Prandtl numbers. Dudis & Davis (1971) considered the stability of buoyancy boundary layers using the energy theory. They found that the critical Reynolds numbers based on the energy theory were much lower than those predicted by Gill & Davey, signifying the existence of subcritical instability of such flows. Iyer & Kelly (1978) performed a weakly nonlinear analysis of the buoyancy boundary layer, assuming two-dimensional disturbances, and

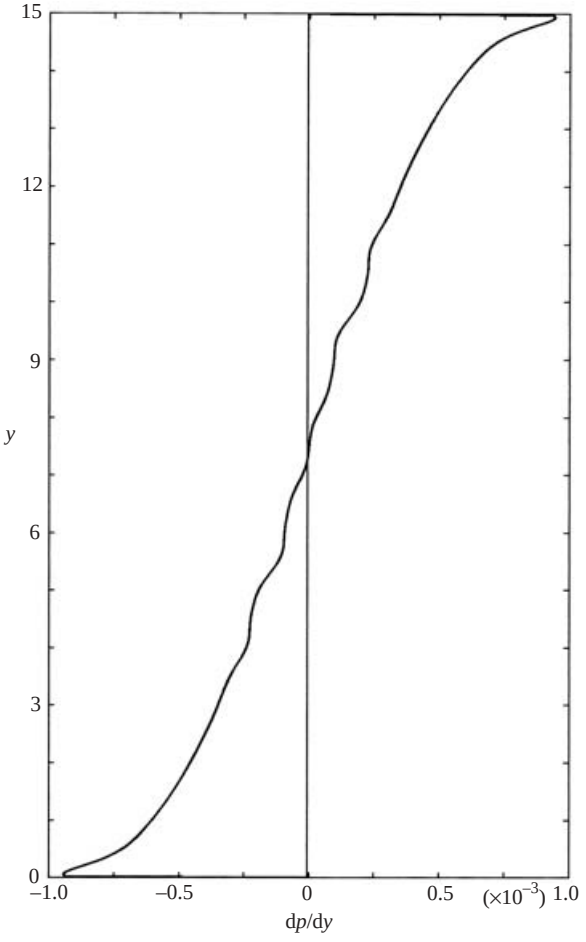

FIGURE 16. Vertical pressure gradient for $Gr = 30\,000$ at $t = 21.0$.

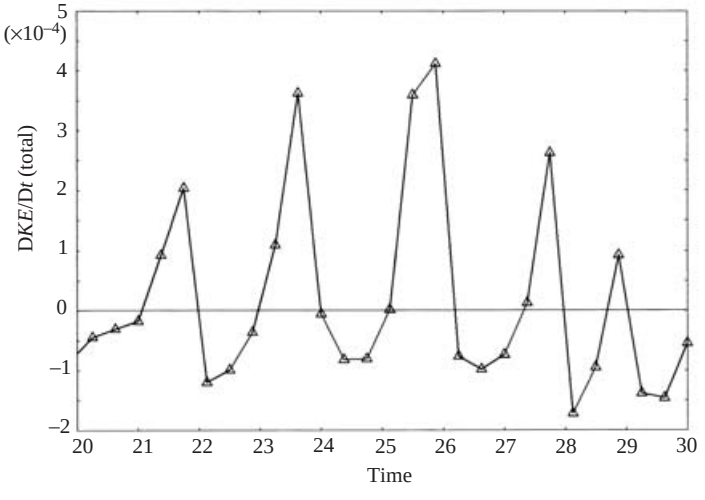

FIGURE 17. Time variation of the rate of change of the total kinetic energy in the tank for $Gr = 30\,000$.

found that the instability was supercritical. Subcritical instability may still exist for three-dimensional disturbances. In terms of experiments, whether the instability is sub- or supercritical, once onset, it should lead to its detection if the instrumentation is appropriately precise. Since the instability is convective in nature, the growth rate should be large enough for the disturbance to grow into a detectable magnitude within the tank. If the instability is subcritical, it may affect the reproducibility of the data depending on the background perturbation present in the flow field.

With the results of the energy analysis of the multicellelar convection state, we can offer a reasonable explanation of the absence of travelling-wave instability in fluids of $Pr \geqslant 12.5$ in convection experiments carried out heretofore. The linear stability analyses carried out by the various authors cited in this paper predicting the onset of travelling-wave instability were all made under the assumption that the pressure in the vertical tank is hydrostatic. This is definitely not the case in a closed convection tank. Because of the motion of the fluid, the dynamic pressure decreases from the two ends to reach a minimum at the centre of the tank. We have shown that the pressure work, although of small magnitude compared to the buoyancy and shear work, contributes importantly to the genesis and subsequent merging of the cells. It is reasonable to conjecture that the existence of a dynamic pressure gradient within the tank suppresses the onset of the travelling-wave mode of instability. If experiments were carried out in tanks with a large enough aspect ratio such that pressure gradient is nearly zero over a considerable length in the middle part of the tank, then travelling-wave instability would develop and be detected.

8. Conclusions

This work was originally undertaken to establish a database of instability characteristics of natural convection in a vertical tank under steady gravity for the purpose of comparing data to be obtained in the same test tank under gravity modulation. As often is the case, a supposedly well-researched phenomenon turned out to have unresolved problems. The results of our work are summarized below.

Experimental results show that for the tested ethanol–water solution with $Pr = 26$, the critical $Gr_{CE} \cong 13\,500$ when multiple convection cells appear in the mid-portion of the tank. At the low supercritical $Gr = 15\,800 \sim 1.17 Gr_{CE}$, cells are observed to merge periodically. This process is examined in detail at $Gr = 20\,800 \sim 1.54 Gr_{CE}$. It is found that convection cells are generated periodically at the upper and lower portions of the tank, and they migrate toward the centre. This converging motion causes the cells in the middle to merge periodically with a period of 7–8 min. Tertiary cells are detected at $Gr = 36\,000 \sim 2.67 Gr_{CE}$, and at $Gr = 54\,100$, they are observed to participate in the merging process. Travelling waves going upward (downward) along the hot (cold) wall are first noticed at $Gr = 64\,400 \sim 4.77 Gr_{CE}$ with a speed of approximately $7\,\mathrm{mm\,s^{-1}}$. The flow becomes turbulent at $Gr = 99\,300 \sim 7.36 Gr_{CE}$.

A two-dimensional simulation of a Boussinesq fluid with constant thermophysical properties shows that the critical $Gr_{CS} = 18\,500$, above which the flow consists of one to three convection cells. The simulations are carried out with 65×1025 grids, much larger than those used in previous investigations. Besides the two-dimensionality and constant properties, the difference between the simulation and experimental results may be also due to the 'background' perturbations in the simulations that are lower than those in the experiments. Simulation results at the same Grashof number ratio (i.e. Gr/Gr_{CS} for the simulation and Gr/Gr_{CE} for the experiment) of ~ 1.6 show cell-merging characteristics similar to those observed in the experiment. By analysing the

rate of change of the kinetic energy of the fluid using the mechanical energy equation, it was found that the source of energy for the cell generation process is provided by the pressure work. Small disturbances present in the tank are being amplified by the pressure work to develop into convection cells. Once developed, these cells derive their energy mainly from the buoyancy work, and they migrate down the pressure gradient toward the middle of the tank and cause the merging of cells there. As the cells merge, the region of strong shear between the cells is eliminated, thereby reducing the dissipation. As a result, the rate of change of the kinetic energy of the fluid assumes a local maximum at the time of merging.

The financial support provided by NASA Grant NAG3-2354 for this work is gratefully acknowledged. We also wish to thank all the referees for their many helpful comments.

REFERENCES

Arakawa, A. 1966 Computational design for long-term numerical integration of the equations of fluid motion: two-dimensional incompressible flow. Part I. *J. Comput. Phys.* **1**, 119–143.

Bergholz, R. F. 1978 Instability of steady natural convection in a vertical fluid layer. *J. Fluid Mech.* **84**, 743–768.

Chen, C. F. & Thangam, S. 1985 Convective stability of a variable-viscosity fluid in a vertical slot. *J. Fluid Mech.* **161**, 161–174.

Chen, W.-Y. & Chen, C. F. 1999 Effect of gravity modulation on the stability of convection in a vertical slot. *J. Fluid Mech.* **395**, 327–344.

Chen, Y.-M. & Pearlstein, A. J. 1989 Stability of free-convection flows of variable-viscosity fluids in vertical and inclined slots. *J. Fluid Mech.* **198**, 513–541.

Christov, C. I. & Homsy, G. M. 2001 Nonlinear dynamics of two-dimensional convection in a vertically stratified slot with and without gravity modulation. *J. Fluid Mech.* **430**, 335–360.

Daniels, P. G. 1987 Convection in a vertical slot. *J. Fluid Mech.* **176**, 419–441.

Dudis, J. J. & Davis, S. H. 1971 Energy analysis of the buoyancy boundary layer. *J. Fluid Mech.* **47**, 381–403.

DuFort, E. C. & Frankel, S. P. 1953 Stability conditions in the numerical treatment of parabolic differential equations. *Math. Tables Other Aids Comput.* **7**, 135–152.

Elder, J. W. 1965*a* Laminar free convection in a vertical slot. *J. Fluid Mech.* **23**, 77–98.

Elder, J. W. 1965*b* Turbulent free convection in a vertical slot. *J. Fluid Mech.* **23**, 99–111.

Ghia, U., Ghia, K. N. & Shin, C. T. 1982 High-*Re* solutions for incompressible flow using the Navier–Stokes equations and a multi-grid method. *J. Comput. Phys.* **48**, 387–411.

Gill, A. E. 1966 The boundary-layer regime for convection in a rectangular cavity. *J. Fluid Mech.* **26**, 515–536.

Gill, A. E. & Davey, A. 1969 Instabilities of a buoyancy-driven system. *J. Fluid Mech.* **35**, 775–798.

Gill, A. E. & Kirkham, C. C. 1970 A note on the stability of convection in a vertical slot. *J. Fluid Mech.* **42**, 125–127.

Hart, J. E. 1971 Stability of the flow in a differentially heated inclined box. *J. Fluid Mech.* **47**, 547–576.

Hollands, K. G. T. & Konicek, L. 1973 Experimental study of the stability of differentially heated inclined air layers. *Intl J. Heat Mass Transfer* **16**, 1467–1476.

Houstis, E. N. & Papatheodorou, T. S. 1979 High-order fast elliptic equation solvers. *ACM Trans. Math. Software* **5**, 431–441.

Iyer, P. A. & Kelly, R. E. 1978 Supercritical solutions for the buoyancy boundary layer. *Trans. ASME* C: *J. Heat Transfer* **100**, 648–652.

Jin, Y. Y. & Chen, C. F. 1996 Instability of convection and heat transfer of high Prandtl number fluids in a vertical slot. *Trans. ASME* C: *J. Heat Transfer* **118**, 359–365.

Landolt, H. & Bornstein, R. 1989 Eigenschaften der Materie in ihren aggregatzustaden, part 5, p. 640. Springer.

Le Quéré, P. 1990 A note on multiple and unsteady solutions in two-dimensional convection in a tall cavity. *Trans. ASME* C: *J. Heat Transfer* **112**, 965–974.

Lee, Y. & Korpela, S. A. 1983 Multi-cellular natural convection in a vertical slot. *J. Fluid Mech.* **126**, 91–121.

Prandtl, L. 1952 *Essentials of Fluid Dynamics*. Blackie.

Roache, P. J. 1982 *Computational Fluid Dynamics*. Hermosa.

Seki, N., Fukusako, S. & Inaba, H. 1978 Visual observation of natural convective flow in a narrow vertical cavity. *J. Fluid Mech.* **84**, 695–704.

Vest, C. M. & Arpaci, V. S. 1969 Stability of natural convection in a vertical slot. *J. Fluid Mech.* **36**, 1–15.

Wakitani, S. 1994 Experiments on convective instability of large Prandtl number fluids in a vertical slot. *Trans. ASME* C: *J. Heat Transfer* **116**, 120–126.

Wakitani, S. 1996 Formation of cells in natural convection in a vertical slot at large Prandtl number. *J. Fluid Mech.* **314**, 299–314.